Journal of Materials Chemistry A



PAPER

View Article Online View Journal | View Issue



Cite this: J. Mater. Chem. A, 2024, 12,

Understanding the fast kinetics and mechanism of sodium storage in antimony using ab initio grand canonical Monte Carlo simulation and operando Xray scattering*

Manni Li,‡^{ad} Tian Qiu, (1)‡^{bc} Samuel S. Welborn, ac Alexandre C. Foucher, Jintao Fu, a Benjamin K. Lesel, e Zeyu Wang, paf Lin Wang, a Eric A. Stach, ac Andrew M. Rappe **D * and Eric Detsi **D **ac

Sodium-ion battery (SIB) alloy anodes are attractive for their high gravimetric capacities, but they suffer from sluggish kinetics during charge storage caused by bulk diffusion during (de)sodiation-induced phase transformations. Among these SIB alloy anodes, antimony (Sb) exhibits one of the fastest (de)sodiation kinetics, with a rate capability comparable to that of intercalation electrodes. It is desirable to understand the origin of Sb fast kinetics, and herein, we use ab initio grand canonical Monte Carlo (ai-GCMC) to predict possible intermediate compounds that form during (de)sodiation of Sb and discover a family of layered glassy intermediates that are not only close to the convex hull of the Na-Sb phase diagram, but are also similar in composition, structure, and energy, suggesting that an amorphous phase may be observed during (de)sodiation. Further, we find that the diffusion barrier for Na in an amorphous/glassy phase can be as low as 6 kJ mol⁻¹. To experimentally validate our simulation results, we performed electrochemical studies including cyclic voltammetry (CV)-based kinetics analysis, which revealed a fast intermediate reaction; and operando wide-angle X-ray scattering (WAXS), which showed an alternating crystalline pattern indicative of an amorphous intermediate. Based on our results, we propose the following sodiation pathway: Sb (crystalline) → Na_vSb (amorphous/glassy) → Na_xSb (amorphous/glassy) \rightarrow Na₃Sb (crystalline), where y < 1.5, $1.5 \le x \le 2$, and these amorphous/glassy intermediate phases are responsible for the fast kinetics.

Received 8th November 2023 Accepted 6th January 2024

DOI: 10.1039/d3ta06832c

rsc.li/materials-a

Introduction

Energy storage technologies beyond lithium-ion batteries (LIBs) are desirable for grid-scale storage of surplus electricity from intermittent resources such as wind and sunlight. The abundance of sodium makes rechargeable sodium-ion batteries (SIBs) a promising alternative to LIBs. 1-3 However, progress towards practical SIBs is partly hindered by the lack of SIB anodes that can

sustain high reversible capacities over hundreds of cycles at relatively high current densities (i.e., high rate).4-8 The commonly used hard carbon SIB anode suffers from large initial irreversible capacities.9 Recently, high-capacity alloy anodes such as phosphorus — P (capacity 2596 mA h g^{-1} for the Na₃P phase), tin —Sn (capacity 847 mA h g^{-1} for the Na₃Sn phase), antimony — Sb (capacity 660 mA h g⁻¹ for the Na₃Sb phase), and germanium — Ge (capacity 590 mA h g^{-1} for the amorphous Na_{1.6}Ge phase) have been widely investigated as alternative SIB alloy anodes. 10-26 Among them, Sb stands out for its relatively high capacity retention at high current densities, as illustrated in Fig. 1, which shows the typical gravimetric capacities of state-of-the-art SIB alloy anodes as a function of the current density as reported in the literature. To ensure a fair comparison, alloy anodes in Fig. 1 are based on pure elements rather than composite materials (for example, P is not included, because most reports on P anodes use P/carbon composites, instead of pure P, to enhance the electrical conductivity of P, which is an insulator in nature).27,28 Also, the anode materials in Fig. 1 were investigated using conventional SIB electrolytes instead of new classes of electrolytes with enhanced performance.29-31 It is obvious from Fig. 1 that Sb (red) better

^aDepartment of Materials Science & Engineering, University of Pennsylvania, Philadelphia, Pennsylvania 19104, USA. E-mail: detsi@seas.upenn.edu

^bDepartment of Chemistry, University of Pennsylvania, Philadelphia, Pennsylvania 19104-6323, USA. E-mail: rappe@sas.upenn.edu

eVagelos Institute for Energy Science and Technology (VIEST), Philadelphia, Pennsylvania 19104, USA

^dAutomoive Engineering Research Institute, Jiangsu University, Zhenjiang 212013,

eNanoDian, Los Angeles, California 90095, USA

^fSchool of Materials Science & Engineering, Jiangsu University, Zhenjiang 212013,

[†] Electronic supplementary information (ESI) available. See DOI: https://doi.org/10.1039/d3ta06832c

[‡] Equal contribution.

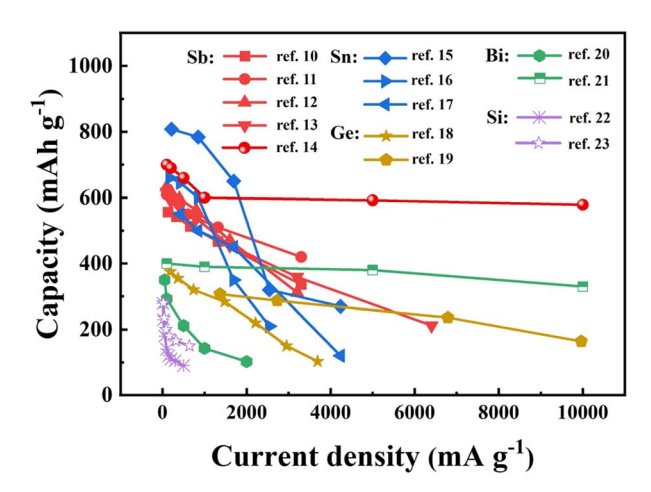


Fig. 1 The rate performance of Sb and other alloy anodes for SIBs selected from literature.

sustains a high capacity at high current densities. For example, while the initial capacity of Sn (blue) is comparable to Sb, at high current densities Sn exhibits rapid capacity loss. In addition, it is worth emphasizing that even bulk Sb (i.e., Sb without nanoscale features) exhibits a high-rate performance. For example, bulk Sb with particle sizes up to tens of micrometers was reported by Darwiche et al. 32 to deliver a capacity of 372 mA h g^{-1} — 56% of the theoretical capacity of Sb — at a C-rate of 4C after 80 cycles. Such remarkable performance in a bulk alloy anode, in which solid-state diffusion and multiple phase transformations are expected to render the kinetics sluggish, raises an intriguing question about the origin of this fast rate and the underlying charge storage mechanism. Therefore, the present work is a fundamental study aimed at elucidating the origin and mechanism of the fast Na storage kinetics in Sb. In doing so, we will build upon pioneering works in the field, on the impact of amorphous phases on charge storage kinetics. For example, the work of Xu et al.33 on amorphized Si nanoparticles and Abel et al.19 on amorphized Ge revealed that amorphous phases can lead to enhanced charge storage performance compared to their crystalline counterparts. In the case of Sb, we hypothesize that although a pristine Sb and fully sodiated Sb (Na₃Sb) electrode materials are both crystalline, there may exist intermediate amorphous phases occurring during Na storage in crystalline Sb (rhombohedral) to form crystalline Na₃Sb (hexagonal), which are responsible for the fast kinetics. In this work, we will verify our hypothesis and shed new light on the kinetics and mechanism of Na storage in Sb using ab initio Grand Canonical Monte Carlo (ai-GCMC) simulation,34 kinetics analysis based on cyclic voltammetry (CV) measurements, and operando wide-angle X-ray scattering (WAXS).

2. Results and discussion

2.1 Theoretical predictions

The previously developed *ab initio* grand canonical Monte Carlo (ai-GCMC) scheme³⁴ is designed to search for the most stable phases of an open system under different chemical potential, which is an ideal tool to explore the intermediates in the (de)sodiation process,

where the number of Na in the system is controlled by its chemical potential. Since the original ai-GCMC method aims to find the stable surface reconstructions from a slab geometry that does not directly apply to the (de)sodiation problem that we are interested in, a revision has been made to extend this scheme to study the cases where the volume of the system is allowed to change. We have derived the detailed balance criteria for the Monte Carlo simulation under the ensemble where the chemical potential of Na, μ_{Na} , the number of Sb, N_{Sb} , the external pressure p, and the temperature, T, are given. More details are provided in the ESI.† Simulations using this scheme were performed under different conditions, where 21 values of μ_{Na} were evenly selected from -2.0 eV to 0.0 eV with bulk Na as the reference. The number of Sb in each simulation cell is fixed at 8 without external pressure and the temperature is 298 K. A refined search was further performed with μ_{Na} ranging from -1.85 eV to -1.25 eV with an increment of 0.03 eV. For each choice of μ_{Na} , two simulations were performed, with the initial structure being Sb and Na₃Sb, respectively. All structures that were sampled in the simulations were collected, and the most energetically favored structures at different compositions were selected to construct the convex hull plot, which is shown in Fig. 2.

Since the ai-GCMC method aims to find the most thermodynamically stable structure at each chemical potential condition, it is expected that NaSb and Na₃Sb are the only two vertices of the convex hull plot, and both of them are in their crystalline structure. Our results, however, suggest the existence of an amorphous/ glassy phase that can be easily reached in the composition range from Na_{1.5}Sb to Na₂Sb. To be specific, the simulation discovered several quasi-stable structures in this composition range whose energies are both very close to each other, and to the convex hull. Their energies above the convex hull are listed in Fig. 2b. Such a small energy penalty suggests that these structures can be thermodynamically visited at room temperature. More importantly, these phases share the same structural motif, as shown in Fig. 3: the Sb atoms (purple) are dimerized and aligned to each other, surrounded by Na (red) atoms that forms a honeycomb-like environment from the top view. The seemingly over-populated Na atoms in the honeycomb network are from two different layers. The side view from another perspective (not shown) suggests that structures in Fig. 3a-d can be understood as layered glassy structure of Na atoms weaved by Sb atoms in the perpendicular direction. The phonon dispersion calculations (see Fig. S6 in ESI†) suggest that almost all structures in Fig. 3 are dynamically stable except Na15Sb8, which does not change the main observation of this structural motif. The similarity in both structure and energy across a variety of compositions provides room for the formation of amorphous structure that the system can easily reach.

To verify that a nonstoichiometric, amorphous structure can be responsible for fast (de)sodiation, we have also calculated the Na diffusion barrier. We chose the structure in the middle of the composition range that Fig. 3 displays, *i.e.*, Na_{1.75}Sb (Na₁₄Sb₈). The diffusion barrier is evaluated through the nudged elastic band (NEB) scheme for different choices of Na diffusion channels, each with 17 images. We discovered a Na channel, shown in Fig. 4a–f, with a diffusion barrier of \approx 60 meV per diffusing Na atom, *i.e.*, \approx 6 kJ mol⁻¹. Since a compressive strain may exist in the real system, we studied the strain dependence of the diffusion barrier,

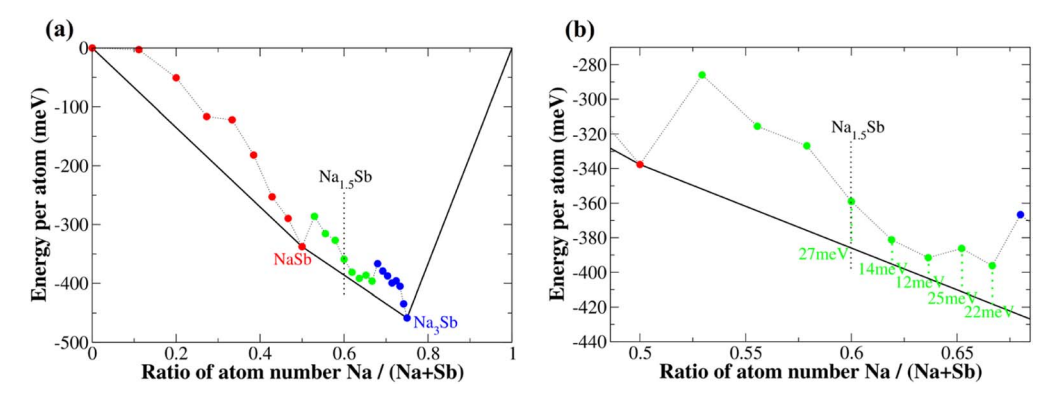


Fig. 2 Convex hull plot predicted by the ai-GCMC simulation. The energy is referred to the energy of the stable bulk Sb and bulk Na. Red dots: compositions from Na_0Sb to Na_1Sb . Green dots: compositions from $Na_{9/8}Sb$ to Na_2Sb . Blue dots: compositions from $Na_{17/8}Sb$ to Na_3Sb . (b) is the zoomed-in view of (a) in the Na_{9/8}Sb to Na₂Sb region.

the results of which are shown in Fig. 4g. A small strain allows more interaction between the Na atoms and the surrounding atoms at the transition state, reducing the diffusion barrier to \approx 40 meV per diffusing Na atom (\approx 4 kJ mol⁻¹). As the strain increases, a new minimum is created along the reaction pathway, and the energy of the transition state increases. Notably, the diffusion barrier is no greater than 60 meV per diffusing Na atom even when 10% strain is applied in all directions, i.e., 27% compression of the total volume. Such a small diffusion barrier and strong tolerance to strain lays a foundation for fast (de) sodiation kinetics.

2.2 Experimental validation

To validate the ai-GCMC simulation results, SIB half-cells consisting of nanoporous Sb (NP-Sb) used as the working electrode, versus Na metal used as the counter and reference electrodes,

were assembled and investigated. Various electrochemical methods including kinetics analysis based on CV measurements and operando WAXS were performed.

2.2.1 Materials characterization. NP-Sb was fabricated by selective removal of manganese (Mn) from an Sb-Mn parent alloy with nominal composition Sb₁₀Mn₉₀ at%, a process known as dealloying. The X-ray diffraction (XRD) data of the asprepared Sb₁₀Mn₉₀ parent alloy shows that it is composed of a Mn phase, marked by the purple stick pattern (PDF #32-0637) in Fig. 5a, and Mn₂Sb intermetallic, marked by the green stick pattern (PDF #04-0822). The XRD pattern of the sample after dealloying (blue curve Fig. 5a) matches very well with the Sb phase, marked by the blue stick pattern (PDF #35-0732).

Nitrogen porosimetry experiments were carried out to confirm that the NP-Sb is indeed porous. The typical nitrogen adsorption/desorption isotherm (Fig. 5b) exhibits type-IV hysteresis behavior, indicating the existence of a mesoporous

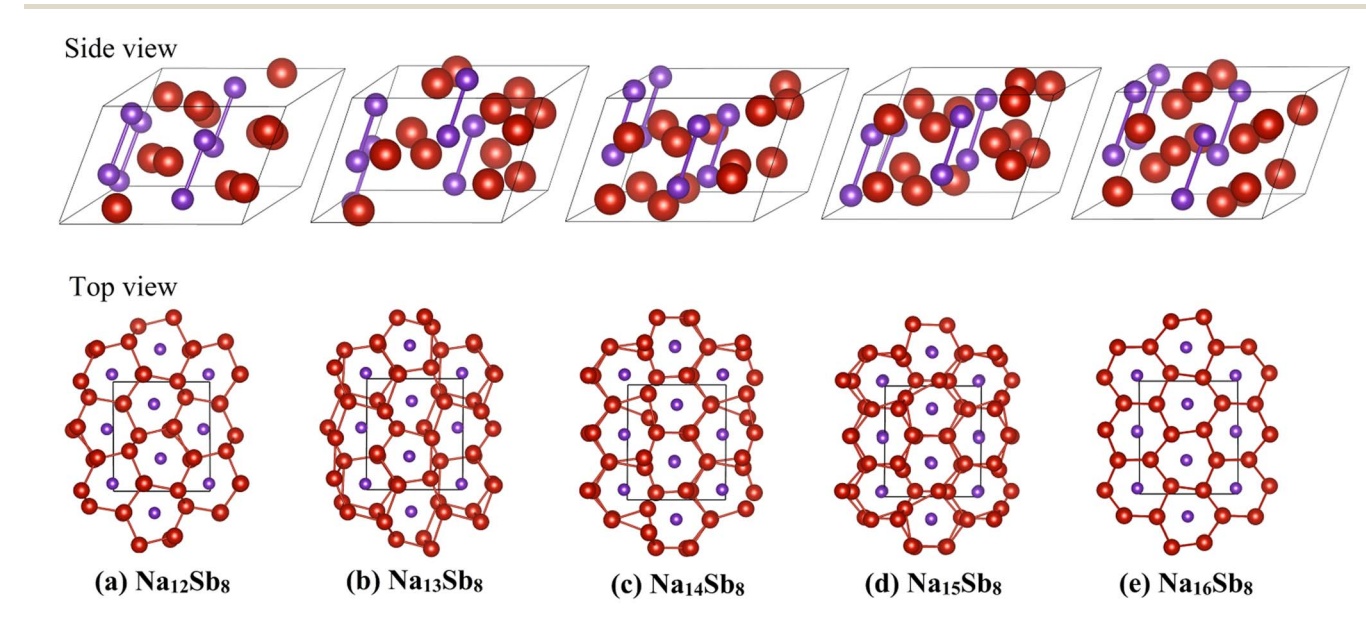


Fig. 3 Structures of selected phases from the convex hull plot. The Na atoms are in red color and the Sb atoms are in purple color. The black boxes indicate the simulation cells. Notice the Sb-Sb dimer in the side view of (a)-(e), and the honeycomb-like structure of Na atoms surrounding the Sb atoms in the top view of (a)-(e).

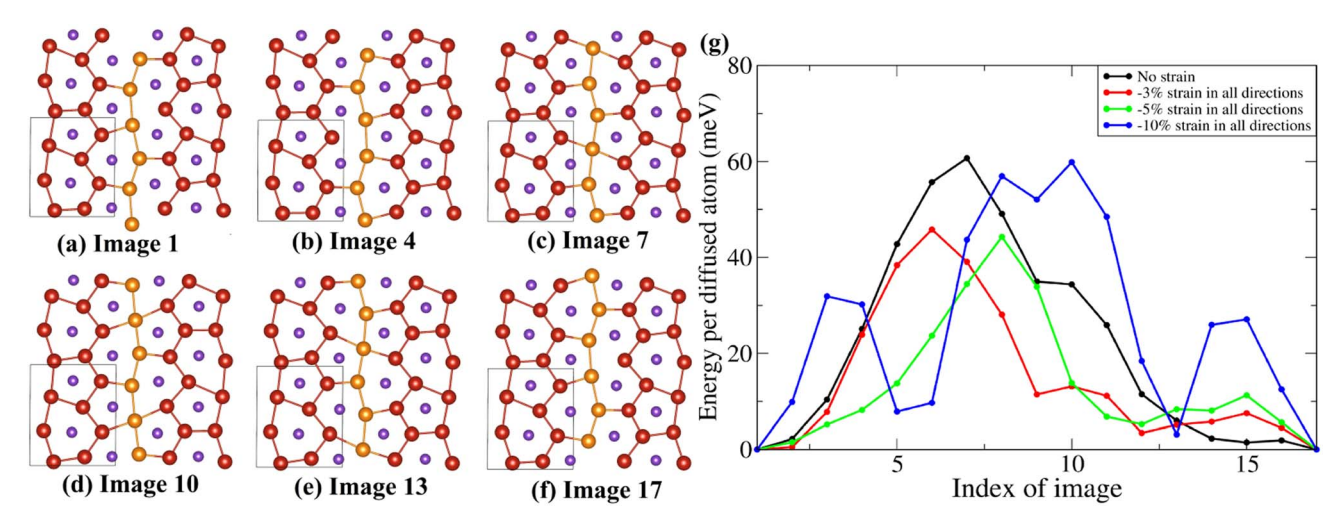
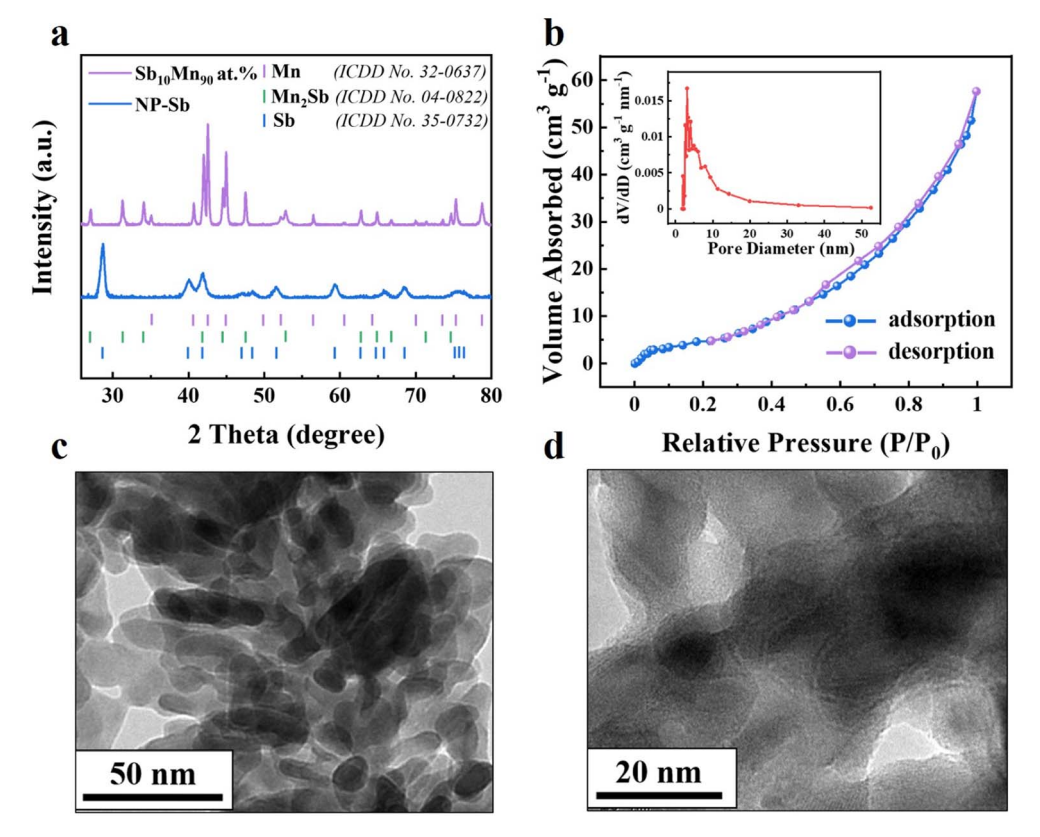


Fig. 4 Fast diffusion of Na. (a-f) The fast Na diffusion channel in Na_{1.75}Sb without strain applied. The diffused Na atoms are in gold color and move upward in the vertical direction. The black boxes indicate the simulation cells from the top view. Since each simulation cell consists of two different Na layers that alternate in the extended cell (along the horizontal direction), each Na layer repeats in every two simulation cell lengths in the horizontal direction in (a-f), and repeats in every one simulation cell length in the vertical direction in (a-f). Note that (f) is identical to (a)except that all diffused Na atoms are moved upward by one bond length distance. (g) Strain-dependent diffusion energy surface of the fast diffusion path.

structure. The specific surface area deduced using the Brunauer, Emmett, and Teller (BET) method is found to be 18 m² g^{-1} . The pore size distribution of NP-Sb (inset of Fig. 5b) is found to be in the range of 3-10 nm.

Transmission and scanning electron microscopy (TEM and SEM) were further used to confirm these structure sizes. Typical TEM images of the dealloyed NP-Sb are shown at different magnifications in Fig. 5c and d, where it is seen that the



 $Fig. 5 \quad \text{(a) XRD patterns of the $Sb_{10}Mn_{90}$ at \% parent alloy (purple curve) and the as-dealloyed sample (blue curve). (b) N_2 adsorption-desorption and the as-dealloyed sample (blue curve) and the as-dealloyed sample (blue curve).}$ isotherms. The inset shows the pore size distribution of NP-Sb. (c) TEM image of NP-Sb at low magnification. (d) TEM image of NP-Sb at high magnification.

ligament/pore size is in the range of ≈ 10 nm, in agreement with nitrogen porosimetry data. SEM images show that the dealloyed sample exhibits a bimodal porosity (see ESI Fig. S1†), as recently reported in our previous work.10 The two phases present in the Sb₁₀Mn₉₀ parent alloy are responsible for this bimodal porosity: the large ligament/pore structures with size between 100-300 nm (Fig. S1a and b†) come from the dissolution of the Mn phase during dealloying, while the mesoscopic ligament/pore structures with size ≈10 nm (Fig. S1c,† 5c and d) come from Mn removal from the Mn₂Sb intermetallic phase.

The chemical composition of the Sb-Mn parent alloy and the corresponding dealloyed NP-Sb were investigated by EDX (Fig. S2 and Table S1†). The atomic ratio between Sb and Mn changes from ≈10:90 before dealloying to ≈98:2 after dealloying (Table S1†), suggesting that Mn was almost fully removed from Sb₁₀Mn₉₀ during dealloying, eventually becoming NP-Sb.

2.2.2 Electrochemical characterization: rate capability, cycle life, and electrochemical impedance spectroscopy. A series of electrochemical tests were carried out to evaluate the rate performance of NP-Sb. Fig. 6a and b show the galvanostatic curves of NP-Sb at various C-rates (Fig. 6a) and the corresponding rate capability (Fig. 6b). Even at a relatively high rate of 5C (which corresponds to charging or discharging in 12 minutes), the material retained a large specific capacity of ≈ 335 mA h g⁻¹, which is over \approx 50% of the theoretical capacity of Sb. While such a rate performance may be expected in intercalation electrode materials, it is unusual in alloy anodes in which charge storage involves bulk diffusion and multiple solid-solid phase transformations. Moreover, since Na atoms are much bigger than Li atoms, in general one would expect the kinetics of Na storage in crystalline Sb (rhombohedral) to form crystalline Na₃Sb (hexagonal) to be more sluggish than Li storage in Sb to form Li₃Sb. Surprisingly, studies have shown that Na and Li storage in Sb exhibit similar kinetics.36 When our C-rate was reduced from 5C to C/5, the capacity recovers to its original value (Fig. 6b), demonstrating charge storage reversibility. Fig. 6c shows the long-term cycle life of the NP-Sb (discharge in blue, charge in purple), demonstrating its excellent cycling stability, with 94% capacity retention after 200 cycles. The corresponding galvanostatic curves for cycles #1, 2, 50, 100, 200 are shown in Fig. 6d. The first discharge curve (black Fig. 6d) displays a long plateau associated with Na storage in Sb as well as irreversible side reactions (solidelectrolyte interphase — SEI — formation) in the first cycle. 37,38 The plateaus in the galvanostatic curves indicate that the charge storage process remains faradaic during long-term cycling.

To verify that Na is uniformly distributed in the bulk of NP-Sb during sodiation, elemental mapping was performed on sodiated NP-Sb samples using scanning transmission electron microscopy (STEM). It can be seen from Fig. 7 that elemental Na and Sb are uniformly distributed through the bulk of the material, confirming that the Sb fully reacts with Na to form Na₃Sb. Electrochemical impedance spectroscopy (EIS) was used to investigate the charge transfer resistance arising during (de)sodiation. The Nyquist plots shown in Fig. S3† consist of depressed semicircles in the high and medium frequency regimes, related to charge transfer resistance, and a linear region related to Warburg diffusion. The larger depressed semicircle diameter ($\approx 700 \Omega$) in the first cycle (red,

Fig. S3†) can be attributed to charge transfer resistance during Na storage and the irreversible side-reactions occurring in the first cycle as mentioned earlier. After the first cycle, the semicircle diameter reduced from $\approx 700 \Omega$ to $\approx 300 \Omega$. This can be explained by the reduction in feature size of the NP-Sb electrode because of the huge volume expansions and structural changes occurring during Na storage in the first few cycles, which causes the material to pulverize, reducing the effective diffusion distance and allowing more electrolyte to wet the void space, thus lowering the charge transfer resistance.39

2.2.3 Operando X-ray scattering and kinetics analysis. Operando WAXS was carried out to validate the prediction from ai-GCMC, i.e., that amorphous intermediate phases exist between crystalline Sb and crystalline Na₃Sb. During operando WAXS (Fig. 8), X-rays from a molybdenum source (Mo K_{α} , $\lambda = 0.7094 \text{ Å}$) interact with the NP-Sb electrode in real-time during (de)sodiation at a constant current density (C/8) in the voltage window between 0.1–1.5 V vs. Na⁺/Na. The cell configuration used for this purpose is shown in Fig. S4.† At the beginning of the reaction, signals of crystalline Sb (rhombohedral, PDF #35-0732) are detected at the 2θ values of ≈13°, ≈18° and ≈19°, as depicted by blue triangle markers in Fig. 8. Two other signals are observed: the signal at the 2θ value of $\approx 12^{\circ}$ marked by a black triangle, which is associated with graphite from the slurry; and the strong signal located at ≈13.5° marked by a red triangle, which is associated with the Na metal used as the counter electrode in the cell. Interestingly, during the first and second sodiation steps, the Sb signals remain at their initial 2θ values as illustrated by the dashed black ovals in Fig. 8. In other words, no new crystalline intermediate phase forms during sodiation; instead, a close look at the Sb signals reveals that the intensity of these Sb signals gradually fades away during sodiation (see for instance the signal at the 2θ value of \approx 13°), suggesting that the fraction of crystalline Sb decreases during sodiation. Thus, since no new crystalline intermediate phase forms during sodiation, the decrease in the Sb signal intensity obviously suggests the formation of an amorphous intermediate that does not give rise to a strong scattering signal during sodiation. Moreover, during sodiation, the signals of crystalline Na₃Sb located at the 2θ values of $\approx 8.5^{\circ}$, ≈ 9.5 , $\approx 15.5^{\circ}$, ≈17.5° and marked by the purple triangles (hexagonal, PDF #01-074-1162) start to appear in the final stage of sodiation, only after the disappearance of the Sb scattering signals. This further indicates that rhombohedral Sb transforms into hexagonal Na₃Sb through the amorphous intermediate phases. During the first and second desodiation steps, the Na₃Sb scattering signals (dashed white ovals in Fig. 8) vanish gradually without observation of new crystalline signals, and only transform back into crystalline Sb signals after the complete disappearance of the Na₃Sb signals, further confirming the formation of the amorphous phase during cycling. The disappearance and reappearance of the scattering signals associated with Sb and Na₃Sb implies that the reversible (de)sodiation processes take place between Sb/Na₃Sb through an amorphous intermediate phase. This result is consistent with the amorphous intermediate phase predicted by ai-GCMC.

CVs of NP-Sb were collected at the scan rates of 0.1, 0.2, 0.5, 1, 2 and 5 mV s⁻¹ (Fig. 9a). During cathodic scans, sodiation of Sb to make Na₃Sb takes place from ≈ 0.7 V down to ≈ 0.1 V.

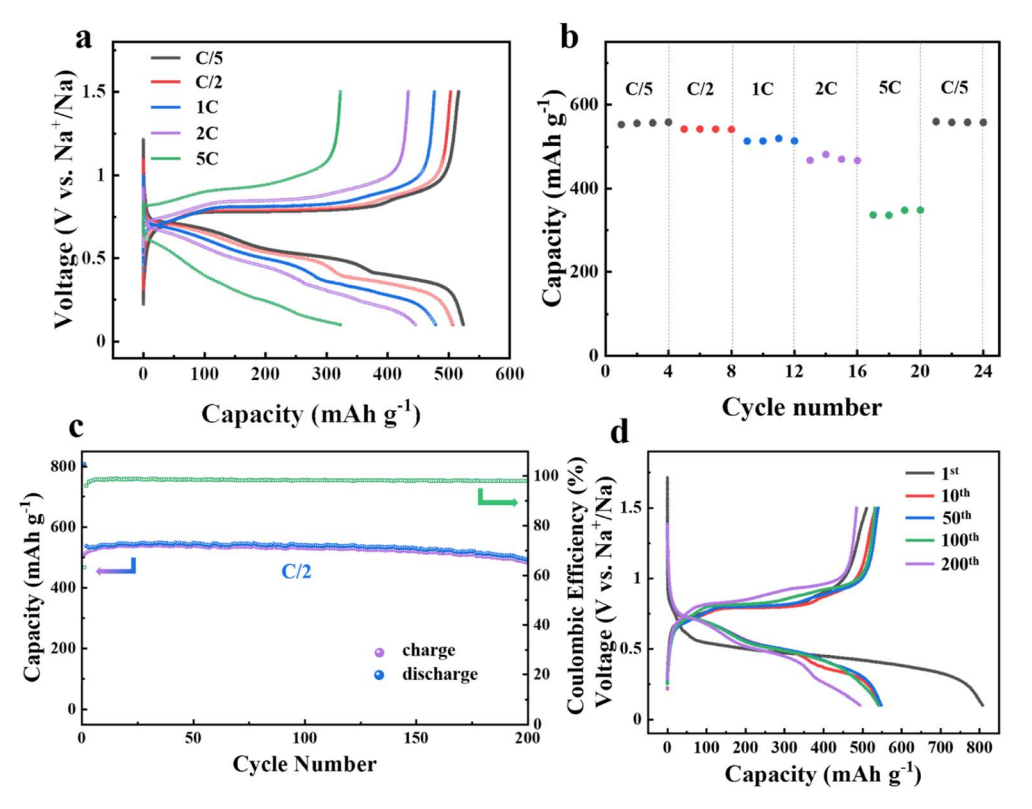


Fig. 6 (a) Galvanostatic charge/discharge curves of NP-Sb at various C-rates. (b) Rate capability of NP-Sb at various C-rates. (c) Cycling performance of NP-Sb at C/2. (d) Corresponding galvanostatic charge/discharge curves of NP-Sb at different cycles.

Because the process involves the transfer of 3 electrons, 3 reduction peaks can be observed (see also Fig. 10a). During anodic scans, desodiation of Na₃Sb takes place from ≈ 0.7 V up to ≈ 1.3 V. Three oxidation peaks can also be expected but these peaks nearly overlap. The relationship between the peak current ($i_{\rm peak}$) and the scan rate (ν) can be expressed as follows:⁴⁰⁻⁴³

$$i_{\text{peak}} = av^b \tag{1}$$

where a and b are empirical constants. The value of b varies between b=0.5 (diffusion-controlled process) and b=1 (capacitive process). Taking the logarithm on both sides of eqn (1), an equivalent equation can be obtained:

$$\log(i_{\text{peak}}) = b \log(v) + b_0 \tag{2}$$

where b_0 is a constant given by $b_0 = \log(a)$. Linear relationships based on the log-log plot of eqn (2) are shown in Fig. 9b for one anodic peak (peak A from Fig. 9a) and two cathodic peaks (peak C_1 and C_2 from Fig. 9a). The slopes of these lines represent the values of b, which were found to be b=0.55 for peaks A and C_1 , b=0.65 for peak C_2 . Comparing the value of b for peak C_1 (which is associated with the first electron transfer during sodiation), and peak C_2 (which is associated with the second electron transfer during sodiation) suggests that the reaction corresponding to peak C_2 exhibits faster kinetics (*i.e.*, since at C_2 the value of b is much higher than 0.5, and the process is not entirely diffusion-controlled).

To further elucidate the fast kinetics of the second sodiation reduction peak, an alternative kinetics analysis was carried out. The total current at a given scan rate contains contributions

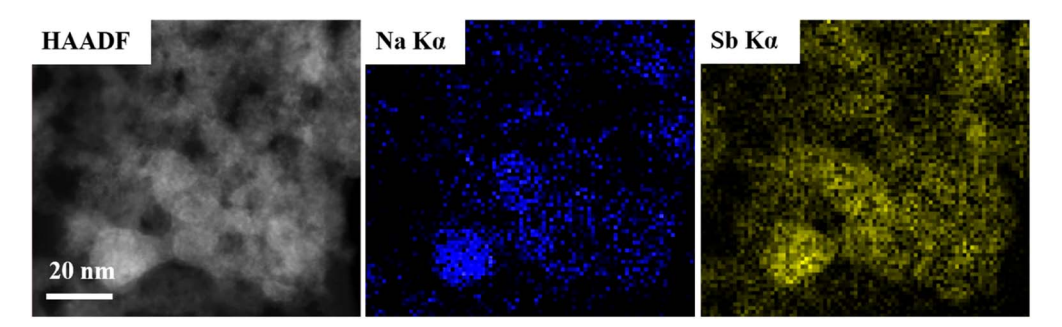


Fig. 7 High-angle annular dark-field imaging (HAADF) and elemental distribution of the electrode after the first sodiation, confirming that Na is distributed uniformly through the bulk of the sodiated electrode.

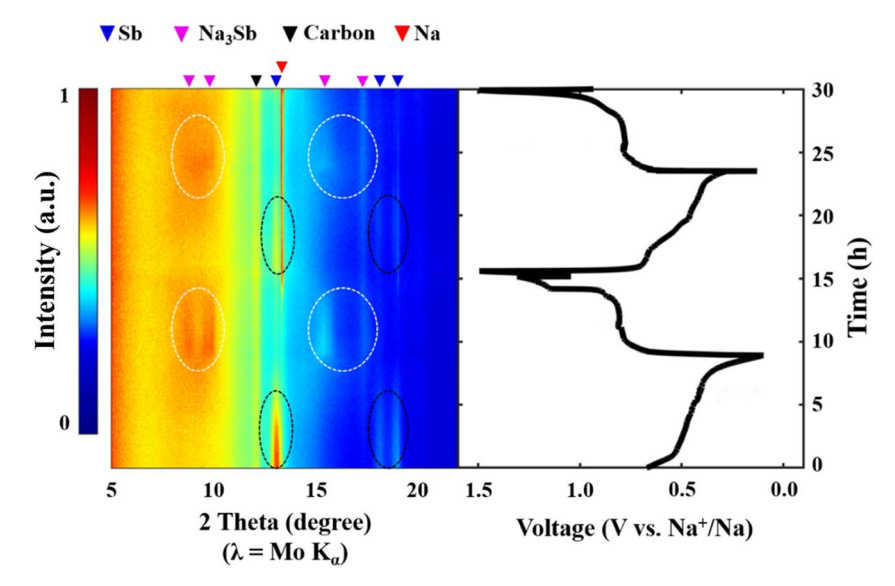


Fig. 8 Surface plot of the operando wide-angle X-ray scattering data of NP-Sb (left) and corresponding galvanostatic curves cycled at C/8 (right).

from both diffusion-controlled processes and capacitive processes, as mentioned earlier.44-46 By fitting the CVs, the ratio of the two contributions can be estimated using eqn (3):47-49

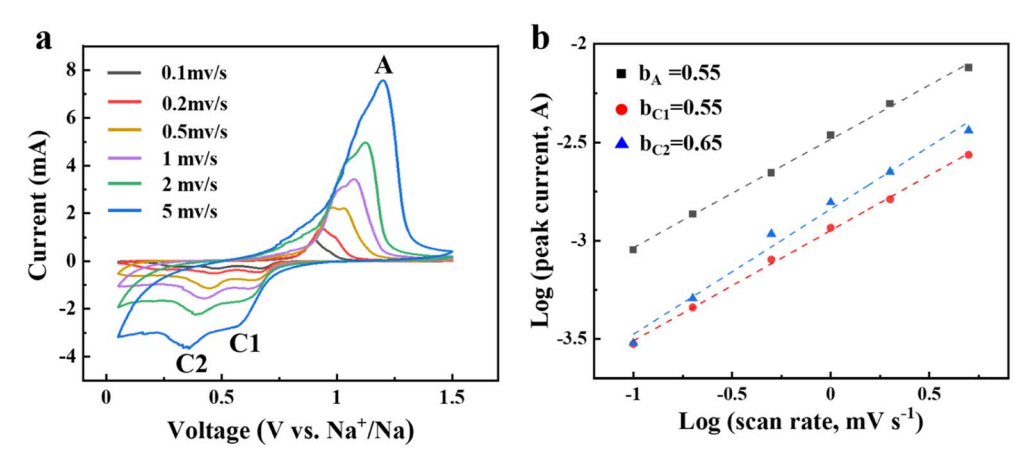
$$i(V, v) = k_1 v + k_2 v^{1/2}$$
(3)

where i is the current at a given potential, k_1v represents the capacitive current and $k_2 v^{1/2}$ represents the diffusion-controlled current. We can rearrange eqn (3) to simplify fitting by dividing both sides by $v^{1/2}$:

$$i(V, v)/v^{1/2} = k_1 v^{1/2} + k_2 (4)$$

Thus, a linear fit of the $i(V, v)/v^{1/2}$ versus $v^{1/2}$ plot will yield k_1 and k_2 as the slope and intercept, respectively. Fig. 10a shows the CV curve of NP-Sb at a scan rate of 0.1 mV s⁻¹ containing a region shaded in red, corresponding to the capacitive contribution to the total current, suggesting that a contribution of 39.2% comes

from the capacitive process. As illustrated in Fig. S5,† the capacitive contribution is 48.5%, 56.1%, 67.8%, 74% and 81.8% at scan rates of 0.2, 0.5, 1, 2, and 5 mV s⁻¹, respectively. Interestingly, we can see from the shaded region in Fig. 10a that there is less capacitive contribution around the first and third redox peaks, with the exception of the second cathodic peak, indicating that the intermediate reduction process during sodiation exhibits faster kinetics than that of the first and third reduction processes, which is in agreement with the results obtained in Fig. 9b and the theoretical prediction that the diffusion barrier in the amorphous phases (Na_{1.5}Sb to Na₂Sb) is small. In summary for this section, three distinct reduction peaks were observed from the CVs during each cathodic scan, indicating that three electrons are involved in the reduction process. The three reduction peaks correspond to the following reaction sequence: Sb \rightarrow Na_vSb \rightarrow Na_xSb \rightarrow Na₃Sb.^{50,51} This sequence is shown schematically in Fig. 10b. The sequence starts from rhombohedral Sb and ends up as hexagonal Na₃Sb,



(a) CVs of NP-Sb anode with different scan rates. (b) The linear relationship between peak current and scan rate in a log-log plot.

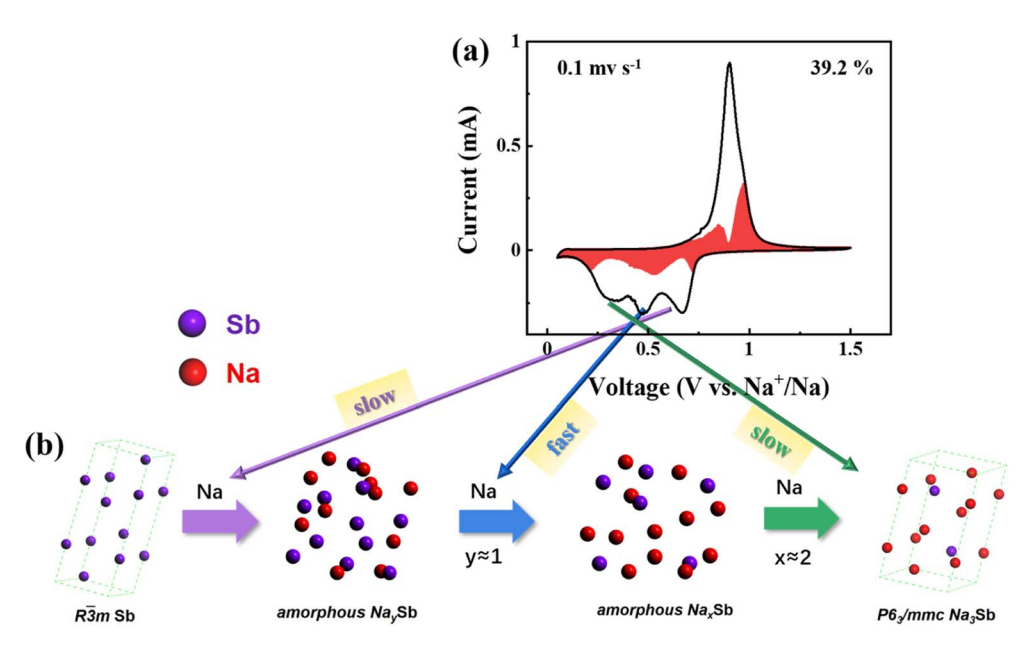


Fig. 10 (a) Capacitive contribution (red region) and diffusive contribution (white region) at 0.1 mV s^{-1} . (b) A schematic of the reaction during sodiation process.

but amorphous phase transformations dominate the intermediate reaction processes rather than crystalline phase transformations.^{32,52,53} On the basis of our kinetics analysis, it is during the amorphous transition that the kinetics are the fastest. Consequently, the fast kinetics of the Sb in SIBs can be attributed to the amorphous phase transformation during cycling.

Conclusions

Sb stands out among SIB alloy anodes for its rate performance, as it can store charge at a rate comparable to that of intercalation materials. In this work, we sought to determine the cause of this outstanding behavior using ai-GCMC simulations, operando WAXS, and kinetics analysis based on CV measurements. Our simulation results suggest the formation of amorphous phase in the composition range of Na_{1.5}Sb to Na₂Sb, and the study of Na diffusion suggests a barrier no greater than 60 meV per diffused atom (\approx 6 kJ mol⁻¹). Our operando WAXS data show that during sodiation, the scattering peak intensity of Sb disappears entirely before scattering peaks of Na₃Sb appear, and vice versa during desodiation. Since no other scattering peaks arose during this process, this pattern suggests the existence of amorphous intermediates between crystalline Sb and Na₃Sb during (de)sodiation. Our kinetics analysis from CV measurements further suggest that, of the three sodiation processes, the second contains a significant capacitive contribution indicative of fast kinetics. Combining this kinetics analysis with the results from ai-GCMC simulation and operando WAXS, we propose the following overall reaction sequence for sodiation of Sb: Sb (crystalline) → Na_vSb (amorphous) → Na_xSb (amorphous) $\rightarrow Na_3Sb$ (crystalline), where the intermediate phase transition (i.e., from amorphous Na_vSb to

amorphous Na_xSb) shows faster kinetics than that of the other transformation processes. Our results provide a better understanding of the fast kinetics in high-rate Sb SIB anodes and highlight the significant impact amorphous phases can have on the electrochemical performance of alloying systems for charge storage.

Methods and experimental section

4.1 Theory

Quantum Espresso was used to perform all DFT calculations, and both ionic positions and lattice constants are allowed to relax. The plane-wave energy cutoff is 60 Ry in all calculations. The generalized gradient approximation of Perdew, Burke, and Ernzerhof was used to treat electron exchange and correlation. Designed nonlocal, optimized, norm-conserving pseudopotentials were generated for Na and Sb using OPIUM. Se, 37 We used 2s, 2p, and 3s as the valence states for Na and 4p, 4d, 5s, and 5d for Sb. The sampling of structures (ai-GCMC step) used a Γ -point calculation with forces converged to 0.1 eV A⁻¹, and structures with the lowest energy at each composition were then further fully relaxed using a $4 \times 4 \times 4$ shifted k-point grid with forces converged to 0.001 eV A⁻¹. For the NEB calculations, the climbing image (CI) technique was applied to the images at energy maxima to refine the prediction of the reaction barrier.

4.2 Materials preparation

The form of Sb used in this work is nanoporous Sb (NP-Sb) fabricated by dealloying, the selective removal of manganese (Mn) from an Sb–Mn parent alloy with nominal composition $\mathrm{Sb_{10}Mn_{90}}$ at%. The $\mathrm{Sb_{10}Mn_{90}}$ parent material was synthesized using an electric arc-melting system (EQ-SP-MSM207 from MTI). Mn powder (Fisher Scientific, 99.99%) and Sb powder

(Fisher Scientific, 99.999%) with an Sb-to-Mn mass ratio of 1: 4.1 were melted into an Sb-Mn alloy ingot in an argon environment. Afterwards, the ingot was crushed into fine powder using a pestle and mortar and immersed in 1 M hydrochloric acid (HCl) solution for 6 hours to fully dissolve the sacrificial Mn component by free corrosion. After dealloying, the dealloyed powders were first rinsed three times with deionized water and subsequently with methanol. The rinsed powders were dried for 12 hours under vacuum and moved into an argonfilled glove box for electrode preparation.

4.3 Materials characterization

X-ray diffraction analysis was performed using a Rigaku Miniflex benchtop X-ray diffractometer equipped with Cu Kα radiation within a 2θ range of 25-80° with 0.02° step size and 2° min⁻¹ scan rate. The morphology of the dealloyed sample was studied by scanning electron microscopy (SEM) JEOL 7500F. Nitrogen sorption measurements were carried out by using a JW-BK132F surface area and porosity analyzer. Scanning transmission electron microscopy (STEM) was performed with an aberration-corrected JEOL NEOARM with a voltage of 200 kV. Energy-dispersive X-ray spectroscopy was analyzed with DigitalMicrograph, a software provided by Gatan Inc; for imaging and spectroscopy, a camera length of 4 cm has been used with a probe current of 150 pA; the samples were diluted in isopropanol and dropcast on lacey carbon films on copper grids (Electron Microscopy Sciences). Operando WAXS was performed using the Mo source on the DEXS instrument at the University of Pennsylvania.

4.4 Electrochemical measurements

The working electrodes were fabricated by mixing 60 wt% active material (the NP-Sb), 30 wt% carbon additives (10 wt% carbon black, 10 wt% carbon nanofibers and 10 wt% graphene nanosheets) and 10 wt% binder (30 mg ml^{-1} of sodium carboxymethyl cellulose dissolved in deionized water) to form a homogenous slurry, which was cast onto a copper foil current collector (Batch No. 0011605, MTI Corp.) using a blade film applicator. The slurry coating was dried under vacuum at room temperature overnight, after which it was heated at 150 °C under an argon atmosphere for 2 hours to remove residual water. After drying, circular disks of the Sb working electrode with active material loading in the range 0.6-1.2 mg cm⁻² were cut with a disc cutter (MSK-T-09, MTI Corp) and assembled into 2032 type coin cells in an argonfilled glove box (MBraun) with water/oxygen content below 0.1 ppm, using sodium metal as the counter and reference electrode and glass microfiber (Whatman, Grade GF/C) as the separator. The electrolyte was 1 M sodium perchlorate in ethylene carbonate (EC)/dimethyl carbonate (DMC) (1:1 by volume) with 5 vol% addition of fluoroethylene carbonate (FEC). All electrochemical tests were performed using a Biologic VMP-300 multichannel potentiostat/galvanostat/EIS. Cyclic voltammetry (CV) measurements were carried out in a voltage window between 0.05 V and 1.5 V vs. Na⁺/Na. Galvanostatic tests were conducted in the voltage window

between 0.1 V and 1.5 V vs. Na⁺/Na at various C-rates. Electrochemical impedance spectroscopy (EIS) data were taken using AC voltage with an amplitude of 10 mV in a frequency range between 1 MHz and 10 mHz.

Conflicts of interest

There are no conflicts to declare.

Acknowledgements

The authors are thankful to the Vagelos Institute for Energy Science and Technology (VIEST) for the financial support through the 2018 VIEST seed grant. This work was carried out in part at the Singh Center for Nanotechnology, part of the Nanotechnology Coordinated Infrastructure Program, which is supported by the NSF grant NNCI-1542153. T. Q. acknowledges the support of the US Department of Energy, Office of Basic Energy Sciences, under grant DE-SC0019281. A. M. R. acknowledges the support of the Army Research Laboratory via the Collaborative for Hierarchical Agile and Responsive Materials (CHARM) under cooperative agreement W911NF-19-2-0119. The authors acknowledge computational support from the National Energy Research Scientific Computing Center. We gratefully acknowledge the financial support from the National Science Foundation (NSF) through the Future Manufacturing Research Grant (FMRG) with award number 2134715, the MRSEC DMR-1720530, and NSF MRI-1725969. The NSF MRI-1725969 grant was used to acquire the Xenocs Xeuss 2.0 Dual Cu-Mo source and Environmental X-ray Source (DEXS) used in this research.

References

- 1 L. Yu, L. P. Wang, H. Liao, J. Wang, Z. Feng, O. Lev, J. S. C. Loo, M. T. Sougrati and Z. J. Xu, Small, 2018, 14, 1-22.
- 2 T. A. Zegeye, M.-C. Tsai, J.-H. Cheng, M.-H. Lin, H.-M. Chen, J. Rick, W.-N. Su, C.-F. J. Kuo and B.-J. Hwang, J. Power Sources, 2017, 353, 298-311.
- 3 L. P. Wang, L. Yu, X. Wang, M. Srinivasan and Z. J. Xu, J. Mater. Chem. A, 2015, 3, 9353-9378.
- 4 J. Ding, H. Wang, Z. Li, A. Kohandehghan, K. Cui, Z. Xu, B. Zahiri, X. Tan, E. M. Lotfabad, B. C. Olsen and D. Mitlin, ACS Nano, 2013, 7, 11004-11015.
- 5 D.-H. Nam, K.-S. Hong, S.-J. Lim, T.-H. Kim and H.-S. Kwon, J. Phys. Chem. C, 2014, 118, 20086-20093.
- 6 M. S. Jo, J. S. Lee, S. Y. Jeong, J. K. Kim, Y. C. Kang, D. W. Kang, S. M. Jeong and J. S. Cho, Small, 2020, 16, 2070207.
- 7 D. H. Youn, H. Park, K. E. Loeffler, J. H. Kim, A. Heller and C. B. Mullins, *ChemElectroChem*, 2018, **5**, 391–396.
- 8 S. Y. Sayed, W. P. Kalisvaart, E. J. Luber, B. C. Olsen and J. M. Buriak, ACS Appl. Energy Mater., 2020, 3, 9950-9962.
- 9 E. Irisarri, A. Ponrouch and M. R. Palacin, J. Electrochem. Soc., 2015, 162, A2476-A2482.

- 10 M. Li, T. Qiu, A. C. Foucher, J. Fu, Z. Wang, D. Zhang, A. M. Rappe, E. A. Stach and E. Detsi, *ACS Appl. Energy Mater.*, 2020, 3, 11231–11241.
- 11 S. Liu, J. Feng, X. Bian, J. Liu and H. Xu, *Energy Environ. Sci.*, 2016, **9**, 1229–1236.
- 12 H. Hou, M. Jing, Y. Yang, Y. Zhang, Y. Zhu, W. Song, X. Yang and X. Ji, *J. Mater. Chem. A*, 2015, 3, 2971–2977.
- 13 H. Li, K. Wang, M. Zhou, W. Li, H. Tao, R. Wang, S. Cheng and K. Jiang, *ACS Nano*, 2019, 13, 9533–9540.
- 14 L. Liang, Y. Xu, C. Wang, L. Wen, Y. Fang, Y. Mi, M. Zhou, H. Zhao and Y. Lei, *Energy Environ. Sci.*, 2015, 8, 2954–2962.
- 15 D.-H. Nam, T.-H. Kim, K.-S. Hong and H.-S. Kwon, *ACS Nano*, 2014, **8**, 11824–11835.
- 16 T.-H. Kim, K.-S. Hong, D. Sohn, M. Kim, D.-H. Nam, E. Cho and H. Kwon, *I. Mater. Chem. A*, 2017, 5, 20304–20315.
- 17 C. Kim, I. Kim, H. Kim, M. K. Sadan, H. Yeo, G. Cho, J. Ahn, J. Ahn and H. Ahn, J. Mater. Chem. A, 2018, 6, 22809–22818.
- 18 A. Kohandehghan, K. Cui, M. Kupsta, J. Ding, E. Memarzadeh Lotfabad, W. P. Kalisvaart and D. Mitlin, *Nano Lett.*, 2014, 14, 5873–5882.
- P. R. Abel, Y.-M. Lin, T. de Souza, C.-Y. Chou, A. Gupta,
 J. B. Goodenough, G. S. Hwang, A. Heller and
 C. B. Mullins, J. Phys. Chem. C, 2013, 117, 18885–18890.
- 20 S. Liu, J. Feng, X. Bian, J. Liu and H. Xu, *J. Mater. Chem. A*, 2016, 4, 10098–10104.
- 21 K. Hu, Y. Chen, C. Zheng, X. Du, M. Wang, Q. Yao, H. Wang, K. Fan, W. Wang, X. Yan, N. Wang, Z. Bai and S. Dou, RSC Adv., 2023, 13, 25552–25560.
- 22 Y. Xu, E. Swaans, S. Basak, H. W. Zandbergen, D. M. Borsa and F. M. Mulder, *Adv. Energy Mater.*, 2016, **6**, 1501436.
- 23 Y. Han, N. Lin, T. Xu, T. Li, J. Tian, Y. Zhu and Y. Qian, *Nanoscale*, 2018, **10**, 3153–3158.
- 24 C. H. Lim, T. Y. Huang, P. S. Shao, J. H. Chien, Y. T. Weng, H. F. Huang, B. J. Hwang and N. L. Wu, *Electrochim. Acta*, 2016, 211, 265–272.
- 25 O. Ruiz, M. Cochrane, M. Li, Y. Yan, K. Ma, J. Fu, Z. Wang, S. H. Tolbert, V. B. Shenoy and E. Detsi, *Adv. Energy Mater.*, 2018, 8, 1801781.
- 26 W. P. Kalisvaart, B. C. Olsen, E. J. Luber and J. M. Buriak, ACS Appl. Energy Mater., 2019, 2, 2205–2213.
- 27 Y. Zhu, Y. Wen, X. Fan, T. Gao, F. Han, C. Luo, S. C. Liou and C. Wang, *ACS Nano*, 2015, **9**, 3254–3264.
- 28 S. Liu, H. Xu, X. Bian, J. Feng, J. Liu, Y. Yang, C. Yuan, Y. An, R. Fan and L. Ci, ACS Nano, 2018, 12, 7380-7387.
- 29 C. Kim, I. Kim, H. Kim, M. K. Sadan, H. Yeo, G. Cho, J. Ahn, J. Ahn and H. Ahn, J. Mater. Chem. A, 2018, 6, 22809–22818.
- 30 J. Huang, X. Guo, X. Du, X. Lin, J.-Q. Huang, H. Tan, Y. Zhu and B. Zhang, *Energy Environ. Sci.*, 2019, **12**, 1550–1557.
- 31 C. Wang, L. Wang, F. Li, F. Cheng and J. Chen, *Adv. Mater.*, 2017, **29**, 1702212.
- 32 A. Darwiche, C. Marino, M. T. Sougrati, B. Fraisse, L. Stievano and L. Monconduit, *J. Am. Chem. Soc.*, 2012, 134, 20805–20811.
- 33 Y. Xu, E. Swaans, S. Basak, H. W. Zandbergen, D. M. Borsa and F. M. Mulder, *Adv. Energy Mater.*, 2016, **6**, 1501436.
- 34 R. B. Wexler, T. Qiu and A. M. Rappe, J. Phys. Chem. C, 2019, 123, 2321–2328.

- 35 G. Henkelman and H. Jónsson, *J. Chem. Phys.*, 2000, **113**, 9978–9985.
- 36 M. He, K. Kravchyk, M. Walter and M. V. Kovalenko, *Nano Lett.*, 2014, **14**, 1255–1262.
- 37 W. Ma, J. Wang, H. Gao, J. Niu, F. Luo, Z. Peng and Z. Zhang, Energy Storage Mater., 2018, 13, 247–256.
- 38 L. Hu, X. Zhu, Y. Du, Y. Li, X. Zhou and J. Bao, *Chem. Mater.*, 2015, 27, 8138–8145.
- 39 J. B. Cook, E. Detsi, Y. Liu, Y.-L. Liang, H.-S. Kim, X. Petrissans, B. Dunn and S. H. Tolbert, ACS Appl. Mater. Interfaces, 2017, 9, 293–303.
- 40 L. Wang, C. Wang, N. Zhang, F. Li, F. Cheng and J. Chen, *ACS Energy Lett.*, 2017, **2**, 256–262.
- 41 Y. Fang, X.-Y. Yu and X. W. Lou, *Angew. Chem., Int. Ed.*, 2018, 57, 9859–9863.
- 42 W. Zhao, L. Zou, X. Ma, W. Zhang, Y. Li, G. Wang, P. Zhang and L. Xia, *Electrochim. Acta*, 2019, **300**, 396–403.
- 43 V. Augustyn, J. Come, M. A. Lowe, J. W. Kim, P.-L. Taberna, S. H. Tolbert, H. D. Abruña, P. Simon and B. Dunn, *Nat. Mater.*, 2013, 12, 518–522.
- 44 J. B. Cook, H.-S. Kim, Y. Yan, J. S. Ko, S. Robbennolt, B. Dunn and S. H. Tolbert, *Adv. Energy Mater.*, 2016, **6**, 1501937.
- 45 G. A. Muller, J. B. Cook, H.-S. Kim, S. H. Tolbert and B. Dunn, Nano Lett., 2015, 15, 1911–1917.
- 46 B. K. Lesel, J. B. Cook, Y. Yan, T. C. Lin and S. H. Tolbert, ACS Energy Lett., 2017, 2, 2293–2298.
- 47 T. Brezesinski, J. Wang, J. Polleux, B. Dunn and S. H. Tolbert, *J. Am. Chem. Soc.*, 2009, **131**, 1802–1809.
- 48 J. Pan, S. Chen, Q. Fu, Y. Sun, Y. Zhang, N. Lin, P. Gao, J. Yang and Y. Qian, *ACS Nano*, 2018, **12**, 12869–12878.
- 49 P. Li, L. Yu, S. Ji, X. Xu, Z. Liu, J. Liu and J. Liu, *Chem. Eng. J.*, 2019, 374, 502–510.
- 50 F. Wan, J.-Z. Guo, X.-H. Zhang, J.-P. Zhang, H.-Z. Sun, Q. Yan, D.-X. Han, L. Niu and X.-L. Wu, ACS Appl. Mater. Interfaces, 2016, 8, 7790–7799.
- 51 J. Duan, W. Zhang, C. Wu, Q. Fan, W. Zhang, X. Hu and Y. Huang, *Nano Energy*, 2015, **16**, 479–487.
- 52 P. K. Allan, J. M. Griffin, A. Darwiche, O. J. Borkiewicz, K. M. Wiaderek, K. W. Chapman, A. J. Morris, P. J. Chupas, L. Monconduit and C. P. Grey, *J. Am. Chem. Soc.*, 2016, 138, 2352–2365.
- 53 W. Ma, J. Wang, H. Gao, J. Niu, F. Luo, Z. Peng and Z. Zhang, Energy Storage Mater., 2018, 13, 247–256.
- 54 P. Giannozzi, O. Andreussi, T. Brumme, O. Bunau, Buongiorno Nardelli, M. Calandra, R. C. Cavazzoni, D. Ceresoli, M. Cococcioni, N. Colonna, I. Carnimeo, A. Dal Corso, S. De Gironcoli, P. Delugas, R. A. Distasio, A. Ferretti, A. Floris, G. Fratesi, G. Fugallo, R. Gebauer, U. Gerstmann, F. Giustino, T. Gorni, J. Jia, M. Kawamura, H. Y. Ko, A. Kokalj, E. Kücükbenli, M. Lazzeri, M. Marsili, N. Marzari, F. Mauri, N. L. Nguyen, H. V. Nguyen, A. Otero-De-La-Roza, L. Paulatto, S. Poncé, Rocca, R. Sabatini, B. Santra, M. Schlipf, A. P. Seitsonen, A. Smogunov, I. Timrov, T. Thonhauser, P. Umari, N. Vast, X. Wu and S. Baroni, J. Phys.: Condens. Matter, 2017, 29, 465901.

- 55 J. P. Perdew, K. Burke and M. Ernzerhof, Phys. Rev. Lett., 1996, 77, 3865-3868.
- 56 N. Ramer and A. Rappe, Phys. Rev. B: Condens. Matter Mater. Phys., 1999, 59, 12471-12478.
- 57 A. M. Rappe, K. M. Rabe, E. Kaxiras and J. D. Joannopoulos, Phys. Rev. B: Condens. Matter Mater. Phys., 1990, 41, 1227-1230.
- 58 G. Henkelman, B. P. Uberuaga and H. Jónsson, J. Chem. Phys., 2000, 113, 9901-9904.